DRAFT VERSION APRIL 29, 2015
Preprint typeset using LaTeX style emulateapj v. 5/2/11

GAMMA-RAY TIMING OF REDBACK PSR J2339–0533: HINTS FOR GRAVITATIONAL QUADRUPOLE MOMENT CHANGES

HOLGER J. PLETSCH[1,2,3] AND COLIN J. CLARK[1,2]

Draft version April 29, 2015

ABSTRACT

We present the results of precision gamma-ray timing measurements of the binary millisecond pulsar PSR J2339–0533, an irradiating system of "redback" type, using data from the *Fermi* Large Area Telescope. We describe an optimized analysis method to determine a long-term phase-coherent timing solution spanning more than six years, including a measured eccentricity of the binary orbit and constraints on the proper motion of the system. A major result of this timing analysis is the discovery of an extreme variation of the nominal 4.6-hour orbital period $P_{\rm orb}$ over time, showing alternating epochs of decrease and increase. We inferred a cyclic modulation of $P_{\rm orb}$ with an approximate cycle duration of 4.2 years and a modulation amplitude of $\Delta P_{\rm orb}/P_{\rm orb} = 2.3 \times 10^{-7}$. Considering different possible physical causes, the observed orbital-period modulation most likely results from a variable gravitational quadrupole moment of the companion star due to cyclic magnetic activity in its convective zone.

Subject headings: gamma rays: stars – methods: data analysis – pulsars: individual (PSR J2339–0533)

1. INTRODUCTION

The Large Area Telescope (LAT; Atwood et al. 2009) on the *Fermi* satellite has paved the way to greatly increase the known Galactic population of compact binary systems harboring irradiating millisecond pulsars (MSP). These intriguing systems are commonly referred to as "black widows" and "redbacks" (Roberts 2013), as the intense pulsar radiation is gradually destroying the companion star. Typically, in black widows the mass of the degenerate companion is very low ($\sim 0.008-0.05\,M_\odot$), whereas the redback type is distinguished by having a non-degenerate, main-sequence-like companion that is more massive ($\sim 0.15-0.6\,M_\odot$). Both types of systems provide interesting opportunities to study the interaction between the pulsar wind and the stellar companion, their unusual formation history (Chen et al. 2013; Smedley et al. 2015) and the evolutionary link to low-mass x-ray binaries (LMXBs) (Archibald et al. 2009; Papitto et al. 2013), as well as the masses of neutron stars (van Kerkwijk et al. 2011; Romani et al. 2012).

Since the launch of *Fermi*, numerous new black widow and redback pulsars were found in targeted pulsar searches of formerly unidentified LAT gamma-ray sources with radio telescopes (e.g., Ransom et al. 2011; Ray et al. 2012; Barr et al. 2013). Only in one case a direct search in LAT data revealed the gamma-ray pulsations of PSR J1311−3430 (Pletsch et al. 2012) by exploiting partial knowledge of the orbit obtained from prior identification of the heated companion at optical and x-ray wavelengths (Romani 2012). Although the pulsar was subsequently detected in the radio band (Ray et al. 2013), it was shown to be weak and intermittent, which had precluded a detection in typical radio searches.

The discovery path to the redback system PSR J2339–0533 followed a similar route. The formerly unidentified LAT source 0FGL J2339.8–0530 was one of the bright gamma-ray sources unveiled during the first 3 months of the *Fermi* mission (Abdo et al. 2009). X-ray and optical follow-up observations identified a probable counterpart, which showed many properties reminiscent of an MSP in a 4.6 hour binary orbit around a low-mass companion (Romani & Shaw 2011; Kong et al. 2012). Only pulsations were lacking for an unambiguous confirmation of the pulsar nature. Using the Green Bank Telescope, Ray et al. (2014, 2015) detected 2.8 ms radio pulsations. They showed that the companion was substantially more massive than modeling of the optical data had initially suggested. With the spin period and orbital parameters tightly constrained, they were also able to detect gamma-ray pulsations with the LAT, verifying the identification of 0FGL J2339.8–0530. Their observed dispersion measure (DM) from the radio detection provided an estimated distance of about 450 pc (Ray et al. 2014, 2015). Up to now, a conjectured variability in the orbital parameters had precluded a phase-coherent ephemeris for the pulsar covering the entire time span of the available LAT data.

Other black widow and redback MSP systems have also been observed to show significant variations in their orbital parameters (Arzoumanian et al. 1994; Doroshenko et al. 2001; Archibald et al. 2013). In the interest of better understanding such phenomena, it is essential to carry out precision timing over longer time intervals (e.g., Nice et al. 2000; Lazaridis et al. 2011). Often the eclipse of the pulsar's radio emission over a large fraction of the orbit additionally complicates or even prohibits an accurate timing analysis of the orbital-parameter variability. On the contrary, the pulsar's gamma-ray emission is essentially unaffected by this problem. Thus, the continuously recorded multi-year LAT survey-mode data is uniquely suited to carefully monitor the long-term evolution of the orbital parameters of those systems.

Here, we present the results of a precision timing analysis of PSR J2339–0533 using LAT gamma-ray photon data that cover more than six years. In Section 2, we describe the data preparation, the improved timing methodology, and provide the details of the inferred phase-coherent pulsar ephemeris. Section 3 provides a detailed discussion of these results. Finally, a summarizing conclusion follows in Section 4.

[1] Max-Planck-Institut für Gravitationsphysik (Albert-Einstein-Institut), D-30167 Hannover, Germany
[2] Institut für Gravitationsphysik, Leibniz Universität Hannover, D-30167 Hannover, Germany
[3] email: holger.pletsch@aei.mpg.de

2. GAMMA-RAY DATA ANALYSIS

2.1. *Data Preparation*

For this analysis we employed Pass 7 reprocessed LAT photon data recorded between 2008 August 4 and 2014 October 17. Via the *Fermi* Science Tools[4] we selected photons belonging to the `P7REP_SOURCE` class with reconstructed directions within 8° of the pulsar position, energies from 0.1 to 100 GeV, and zenith angles $\leq 100°$. Photons recorded when the LAT's rocking angle exceeded 52°or when the LAT was not in nominal science mode were excluded.

We constructed spectral models including all gamma-ray sources found within 13° of the nominal pulsar position from a preliminary version of the third Fermi LAT source catalog (3FGL; Acero et al. 2015) based on four years of LAT data. The parameters were left free only for point sources within the inner 5°. The source models included contributions from the Galactic diffuse emission, the extragalactic diffuse emission, and the residual instrumental background[5]. The pulsar spectrum was modeled as an exponentially cutoff power law, $dN/dE \propto E^{-\Gamma}\exp\left(-E/E_c\right)$, where Γ denotes the spectral index and E_c is the cutoff energy. Using this spectral model of the region and the `P7REP_SOURCE_V15` instrument response functions, we employed `gtsrcprob` to compute a weight for each photon (Kerr 2011), measuring the probability of having originated from the pulsar for further background suppression.

From the final data set we discarded photons with probability weights less than 0.001. While this chosen weight cutoff makes only a negligible change to the significance of the detected pulsations, it dramatically improves the computational efficiency for the subsequent timing analysis.

2.2. *Timing Analysis*

A central aspect of this work is to obtain a precise ephemeris, i.e. a phase-coherent timing solution, covering the full time range of LAT data available. This means counting the exact number of pulsar turns over the past six years of the *Fermi* mission. The initial ephemeris obtained from the radio pulsar discovery using a circular-orbit model was sufficient to reveal significant gamma-ray pulsations (Ray et al. 2014), but was unable to maintain accurate phase coherence over a time span longer than about three years, most likely due to unaccounted orbital variability of the PSR J2339–0533 system. This motivated the present investigation to study and model the putative orbital parameter variation, facilitating a long-term phase-coherent timing solution.

To begin with, we examined the variation of the orbital period $P_{\rm orb}$ and the projected semimajor axis x across neighboring subsets of data. For this, we fixed the sky position to the location of the optical counterpart at $\alpha = 23^{\rm h}39^{\rm m}38\overset{\rm s}{.}75$ and $\delta = -05°33'05\overset{''}{.}3$ (J2000.0) from Romani & Shaw (2011). The remaining pulsar parameters were set to those of the preliminary ephemeris. Assuming a circular orbit we scanned ranges in $\{P_{\rm orb}, x\}$ on a dense grid around their initial values at fixed time of ascending node $T_{\rm ASC}$. At each grid point we computed the weighted H-test statistic (de Jager et al. 1989; Kerr 2011) using photons within a fixed time window of size 110 days. This time window covered almost two precession periods of *Fermi* (56 days) and was chosen by balancing signal-to-noise ratio and time resolution, being just long enough to still accumulate a detectable signal-to-noise ratio. This window was then slid over the entire data set using a 50% overlap between subsequent steps.

The results of this study provided the first evidence that PSR J2339–0533 undergoes alternating intervals of orbital-period increase and decrease, whereas for x no significant variation was observed. To obtain an approximate solution for the evolution of $P_{\rm orb}$ over time, we considered the $P_{\rm orb}$ value giving the highest H-test in each sliding-window step. It became apparent that modeling this set of $P_{\rm orb}$ values over time required us to employ a polynomial expansion of the orbital frequency $f_{\rm orb} = 1/P_{\rm orb}$ about $T_{\rm ASC}$, so that for a given time t the orbital phase $\phi_{\rm orb}$ (measured in cycles) is written as

$$\phi_{\rm orb}(t) = \sum_{k=0}^{K} \frac{f_{\rm orb}^{(k)}}{(k+1)!}\,(t - T_{\rm ASC})^{(k+1)}\,, \tag{1}$$

where $f_{\rm orb}^{(k)}$ represents the kth time-derivative of $f_{\rm orb}$. Simple least-square minimization suggested that the order K needed to give an adequate fit was at least five or six. Ultimately, to determine the model providing the best fit we used the more sensitive timing analysis described next.

As a starting point for the precision timing analysis, we extended the initial pulsar ephemeris by including six orbital-frequency derivatives based on the approximation for the orbital-period evolution of PSR J2339–0533 obtained in the previous step. Since the orbit is apparently of extremely low eccentricity e, we used the Lagrange-Laplace parametrization (Lange et al. 2001) to describe the binary motion with $\epsilon_1 \equiv e\sin\omega$ and $\epsilon_2 \equiv e\cos\omega$, such that $e = (\epsilon_1^2 + \epsilon_2^2)^{1/2}$. The construction of a pulse profile template followed the method of Abdo et al. (2013) extending the work of Ray et al. (2011) by also including the photon weights, labeled w_j for the jth photon. Since this requires a valid ephemeris, we first used only the subinterval (about half) of the full data set over which the initial ephemeris maintained phase coherence for this purpose. In general the pulse profile $F(\phi)$ can be represented by a wrapped probability density function (PDF) of the pulsar's rotational phase $\phi \in [0, 1)$, measured in turns. For PSR J2339–0533, we found that this PDF is well approximated by a sum of a constant background and five unimodal wrapped Gaussian distributions (cf. Abdo et al. 2013). The rotational phase $\phi(t_j, \mathbf{u})$ is a function of the photon arrival time t_j and the vector $\mathbf{u}$ that collects all pulsar spin, positional, and orbital parameters. Thus, to obtain the best-fit values for $\mathbf{u}$ of a given timing model, we evaluated the log-likelihood (Abdo et al. 2013),

$$\log\mathcal{L}(\mathbf{u}) = \sum_{j=1}^{N} \log\left[w_j F(\phi_j(t_j, \mathbf{u})) + (1 - w_j)\right]\,, \tag{2}$$

where N is the total number of gamma-ray photons.

To find the parameters that give the global maximum of the log-likelihood, we followed a novel approach that differs from the method of Ray et al. (2011). Note that in Ray et al. (2011) the LAT data were subdivided into segments in time and over each such segment the photon times were folded using a preliminary ephemeris to obtain a pulse time-of-arrival (TOA) measurement. The set of TOAs from all segments then served as input to a global fitting procedure. Due to the sparseness of the gamma-ray photons, a sufficiently high signal-to-noise ratio for a single TOA determination required long integration times of order weeks. However, this makes it very difficult to

[4] http://fermi.gsfc.nasa.gov/ssc/data/analysis/scitools/overview.html
[5] http://fermi.gsfc.nasa.gov/ssc/data/access/lat/BackgroundModels.html

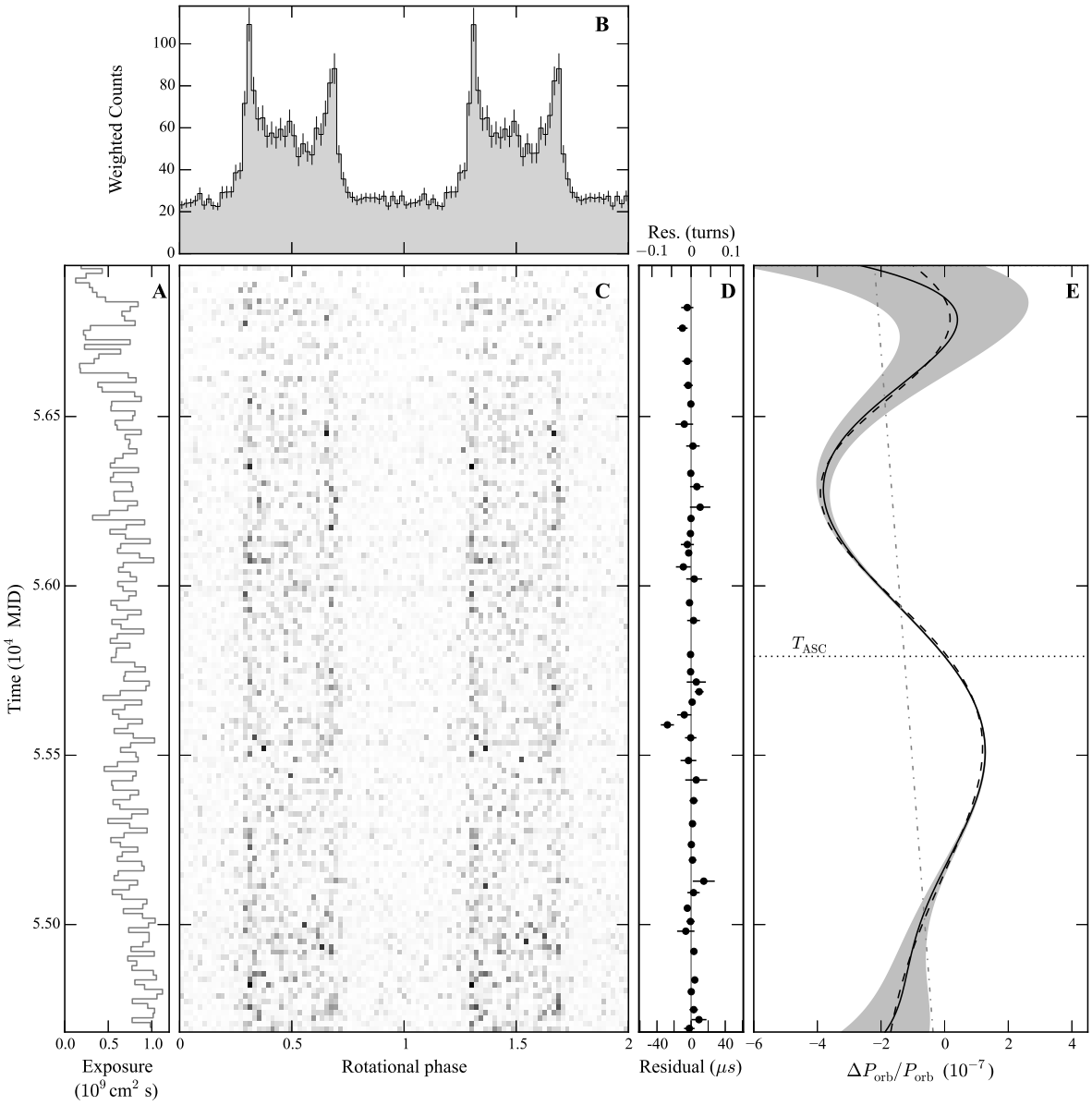

FIG. 1.— Panel A: exposure versus time, binned in steps of 14 days. Panel B: integrated weighted pulse profile, using 50 bins per rotation. The vertical error bars show statistical 1σ uncertainties. Two rotational cycles are shown for clarity. Panel C: two-dimensional weighted histogram of rotational phase versus time, using 140 bins over time. The weighted counts are not exposure-corrected. Panel D: formal timing residuals, where the error bars show statistical 1σ uncertainties. The data points were obtained from non-overlapping subsegments of data that gave approximately the same signal-to-noise ratio (i.e. an H-test value of about 15). Only significant measurements with a log-likelihood greater than 8 were included. Panel E: time evolution of the orbital-period change (solid black curve) based on the timing solution of Table 1 and the surrounding grey-shaded region shows the statistical 1σ uncertainties. The uncertainties increase with the time distance to $T_{\rm ASC}$ (shown by the horizontal dotted line), since the polynomial expansion of the orbital-frequency used in the timing model is about $T_{\rm ASC}$. The dashed curve represents the best-fit cyclic modulation model discussed in Section 3.4 and the dotted-dashed line shows the linearly changing component of this model.

detect effects on much shorter time scales, and orbital parameter variability in particular, since the preliminary ephemeris used to fold the photon times in each segment is not necessarily accurate. Given the pulsed flux level of PSR J2339–0533, one would need segments of duration at least 30 days. For comparison, this interval spans already about 155 orbital revolutions.

Therefore, we instead evaluated the log-likelihood of Equation (2) *directly* using the entire set of unfolded gamma-ray photon times (without binning in time). For the exploration of $\log \mathcal{L}$ over the relevant parameter space of the timing model we employed the Monte Carlo (MC) sampler MULTINEST (Feroz et al. 2009). This multimodal nested sampling algorithm is especially efficient in sampling challenging likelihood surfaces and allows one to calculate posterior distributions as a byproduct.

The timing analysis remains an iterative procedure, specifically since the actual pulse profile is not known a priori. In the first MC run we still held the sky position fixed to the optical-counterpart location (Romani & Shaw 2011), but let the spin and orbital parameters vary. This gave a first phase-connected solution spanning the full LAT data set, from which we then

TABLE 1
PARAMETERS FOR PSR J2339–0533

Parameter	Value
Range of observational data (MJD)	54683 – 56947
Reference epoch (MJD)	55100.0
Timing parameters	
Right ascension, α (J2000.0)	$23^{\rm h}39^{\rm m}38\overset{\rm s}{.}74(1)$
Declination, δ (J2000.0)	$-05^\circ33'05\overset{''}{.}32(3)$
Proper motion in α, $\mu_\alpha \cos\delta$ (mas yr^{-1})	11(4)
Proper motion in δ, μ_δ (mas yr^{-1})	–29(10)
Spin frequency, f (Hz)	346.71337922051(2)
1st spin frequency derivative, $\dot{f}$ (Hz s^{-1})	$-1.6952(8) \times 10^{-15}$
2nd spin frequency derivative, $\lvert\ddot{f}\rvert$ (Hz s^{-2})	$< 2 \times 10^{-26}$
Orbital frequency, $f_{\rm orb}$ (10^{-5} Hz)	5.993873572(1)
1st derivative of orb. frequency, $f_{\rm orb}^{(1)}$ (Hz s^{-1})	$5.97(5) \times 10^{-19}$
2nd derivative of orb. frequency, $f_{\rm orb}^{(2)}$ (Hz s^{-2})	$1.77(4) \times 10^{-26}$
3rd derivative of orb. frequency, $f_{\rm orb}^{(3)}$ (Hz s^{-3})	$-1.06(2) \times 10^{-33}$
4th derivative of orb. frequency, $f_{\rm orb}^{(4)}$ (Hz s^{-4})	$-5.6(2) \times 10^{-41}$
5th derivative of orb. frequency, $f_{\rm orb}^{(5)}$ (Hz s^{-5})	$1.41(5) \times 10^{-48}$
6th derivative of orb. frequency, $f_{\rm orb}^{(6)}$ (Hz s^{-6})	$1.15(6) \times 10^{-55}$
Epoch of ascending node, $T_{\rm ASC}$ (MJD)	55791.9182085(3)
Projected semimajor axis, x (lt-s)	0.611656(4)
Derivative of proj. semimajor axis, $\lvert\dot{x}\rvert$ (lt-s s^{-1})	$< 6 \times 10^{-14}$
1st Laplace-Lagrange parameter, ϵ_1	$1(1) \times 10^{-5}$
2nd Laplace-Lagrange parameter, ϵ_2	$-21(1) \times 10^{-5}$
Derived parameters	
RMS timing residual (μs)	6.7
Spin period, P (ms)	2.8842267415473(2)
1st spin period derivative, $\dot{P}$ (s s^{-1})	$1.4102(6) \times 10^{-20}$
2nd spin period derivative, $\lvert\ddot{P}\rvert$ (s^{-1})	$< 2 \times 10^{-31}$
Orbital period, $P_{\rm orb}$ (d)	0.1930984018(3)
1st derivative of orbital period, $\dot{P}_{\rm orb}$ (s s^{-1})	$-1.66(1) \times 10^{-10}$
Eccentricity, e	$2.1(1) \times 10^{-4}$
Gamma-ray spectral parameters	
Photon index, Γ	1.2 ± 0.3
Cutoff energy, E_c (GeV)	3.7 ± 1.4
Photon flux[a] F_{100} (10^{-8} photons cm^{-2} s^{-1})	2.0 ± 0.2
Energy flux[a] G_{100} (10^{-11} erg cm^{-2} s^{-1})	2.8 ± 0.1

NOTE. — Numbers in parentheses are statistical 1σ uncertainties in the last digits. The JPL DE405 solar system ephemeris has been used and times refer to TDB.
[a] Measured over the energy range from 100 MeV to 100 GeV.

refined the pulse profile template. In the subsequent MC run, we then also let the sky location vary and determined the best-fit values for **u**, from which a further refined pulse profile template was derived for use in the next MC run. Subsequently, we further extended the timing solution to also include additional effects, such as proper motion and orbital eccentricity. We also tested for a variation in the projected semimajor axis, $\dot{x}$, and a second spin-frequency derivative, $\ddot{f}$, but in both cases no significant measurement was made and so we can only give upper limits.

Table 1 presents the final timing solution, obtained after several iterations of pulsar-model and pulse-profile-template refinements. For the best estimate and uncertainty of each parameter in the timing model we report the mean value and standard deviation of the one-dimensional marginalized posterior distribution, as determined by the MULTINEST algorithm. This timing model includes the polynomial expansion of the oscillating orbital frequency as given in Equation (1) truncated at the sixth order ($K = 6$), which gave a maximum $\log\mathcal{L}$ value of about 580.

We also repeated the timing procedure for different models with polynomial expansions truncated at orders $K = 5$ and $K = 7$. To determine which of the three models better fits the data, we then invoked the Bayesian Information Criterion (BIC; Schwarz 1978) as a comparative tool. The BIC value is based on the number of free parameters to be estimated, the number of data points and the maximized value of $\log\mathcal{L}$. The smaller BIC value is preferred, since the BIC becomes increasingly large when either the data is poorly fit or when the number of free parameters increases and the data is overfit. Thus, the BIC is minimized for the simplest model that sufficiently fits the data. In our case, the $K = 7$ model gave about the same $\log\mathcal{L}$ value as for $K = 6$, but given the extra parameter, the simpler $K = 6$ model is preferred according to the BIC. On the other hand, the $K = 5$ model has one parameter less compared to $K = 6$, but gave a significantly lower $\log\mathcal{L}$ value, so that the BIC again preferred the $K = 6$ model. Therefore, we considered the model with $K = 6$ as shown in Table 1 as the optimal representation of the data. However, we also caution that outside the time span of this data, the derived timing solution, specifically the polynomial expansion for the orbital frequency, likely has little predictive power.

2.3. *Timing Results*

In Figure 1, the inferred parameters of the final timing solution of Table 1 were used to generate the integrated pulse profile (panel B), the diagram of rotational phase versus time (panel C), and the residuals over time (panel D). The rectilinearity of the phase tracks over time and the smallness of the residuals clearly certify the phase-coherence of the timing solution, accounting for the correct number of pulsar turns during the observational time span. Merely to illustrate the quality of the timing solution, in Figure 1 (panel D) we also show the phase residuals that have a root-mean-square (RMS) about 1.5% in turn, which translates into an RMS timing accuracy of about 7 μs.

While the sky position of the final timing solution is compatible with the optical counterpart location, we were also able to measure significant values for the proper motion of the system relative to the solar system barycenter (μ_α, μ_δ, given in Table 1). This amounts to a total transverse proper motion of $\mu_t = (\mu_\alpha^2 \cos^2\delta + \mu_\delta^2)^{1/2} \approx (31 \pm 10)$ mas yr^{-1}. Combined with the radio-DM distance estimate of $d = 0.45$ kpc, we derive a transverse velocity of $v_t = d\,\mu_t \approx 30\,{\rm km\,s^{-1}}$. This transverse movement contributes to the observed spin parameters P and $\dot{P}$ due to a changing Doppler shift (Shklovskii 1970) via: $\dot{P} = \dot{P}_{\rm int} + P v_t^2/(dc)$. The latter term, representing the Shklovskii effect, is about 22% of the observed $\dot{P}$, so that the intrinsic spin-period derivative is estimated as $\dot{P}_{\rm int} \approx 1.1 \times 10^{-20}$ s s^{-1}. Hence, we derive a Shklovskii-corrected pulsar spin-down luminosity of $\dot{E} = 4\pi^2 I \dot{P}_{\rm int}/P^3 \approx 1.8 \times 10^{34}$ erg s^{-1}, where $I = 10^{45}$ g cm^2 is an assumed fiducial neutron star moment of inertia.

The timing solution also provides constraints on the companion mass $M_{\rm c}$ through the pulsar mass function by combin-

ing the measurements of x and $P_{\rm orb}$ as

$$f(M_{\rm c}, M_{\rm p}) = \frac{M_{\rm c}^3 \sin^3 \iota}{(M_{\rm c}+M_{\rm p})^2} = \frac{4\pi^2 x^3}{G P_{\rm orb}^2} = (6.58942 \pm 0.00012) \times 10^{-3} M_\odot , \quad (3)$$

where G denotes the gravitational constant, $M_{\rm p}$ labels the pulsar mass, and ι is the inclination angle. When further combined with the optical observations of the companion mass estimates for both components are possible, as will be elucidated in Section 3.1.

We also measured an orbital eccentricity of $e = 2.1(1) \times 10^{-4}$. Given the short 4.6-hour orbital period of PSR J2339–0533, this value of residual eccentricity is higher than predicted by the convective-fluctuation theory of Phinney (1992). This may indicate additional evidence for convective fluctuations in the companion, as we discuss in Section 3.4. While these are perhaps more complicated than assumed by Phinney (1992), they could have inhibited perfect circularization of the binary orbit of PSR J2339–0533.

Most remarkably, the timing solution unveils the extreme orbital-period variations of PSR J2339–0533 over the six years of LAT data. The two most extreme values of the orbital-period derivative attained during this interval are $\dot{P}_{\rm orb} = -5.8 \times 10^{-10}$ s s^{-1} and $\dot{P}_{\rm orb} = 2.7 \times 10^{-10}$ s s^{-1}. Panel E in Figure 1 displays the dramatic evolution of the fractional changes $\Delta P_{\rm orb}/P_{\rm orb}$ based on the ephemeris of Table 1. A significant cyclic modulation of the orbital period is revealed, where the observational interval appears to cover about one and a half cycles. The possible causes of the $P_{\rm orb}$-modulation are discussed in detail in Section 3 below.

3. DISCUSSION

3.1. *Component Masses*

By combining the optical radial velocity measurements of the irradiated companion (Romani & Shaw 2011) and the pulsar ephemeris, further system parameters can be constrained, such as the mass of the pulsar $M_{\rm p}$ and of the companion $M_{\rm c}$. In forthcoming work that will exploit the extremely accurate pulsar mass function when modeling the optical lightcurve, more precise limits on the system parameters will be possible. However, here we employ the previous estimates by Romani & Shaw (2011) in order to obtain fiducial values that are sufficient for the purpose of the subsequent discussion and conclusion as will be shown below.

From radial velocity measurements of the companion, Romani & Shaw (2011) observed a semi-amplitude of $K_{\rm obs} \approx 270\,{\rm km\,s^{-1}}$. While these measurements track the apparent center of light, the radial-velocity amplitude of the companion's center of mass, K_2, can be larger (e.g., van Kerkwijk et al. 2011). The "K-correction" for this effect inferred by Romani & Shaw (2011) gave $K_2 \approx 1.18\,K_{\rm obs} \approx 320\,{\rm km\,s^{-1}}$, which we adopt here. The amplitude of the optical modulation mainly depends on the inclination angle, which Romani & Shaw (2011) estimated as $\iota \approx 60°$. As shown in Figure 2, this gives rise to the following estimates: $M_{\rm p} = 1.48\,{\rm M}_\odot$ and $M_{\rm c} = 0.32\,M_\odot$, that we assume as fiducial values for the rest of this paper. The resulting mass ratio would be $q = M_{\rm p}/M_{\rm c} = 4.61$.

For these mass estimates, the orbital separation is $a \approx 1.71\,R_\odot$ and the companion Roche lobe radius according to Eggleton (1983) is: $R_L \approx 0.88\,R_\odot$. The actual radius of the companion star, $R_{\rm c}$, is difficult to obtain, but can also be estimated from the optical light-curve modeling. In doing so, Romani & Shaw (2011) found that the companion is close to Roche lobe filling, with a filling factor of $R_{\rm c}/R_L \approx 0.9$. Further support for this picture is provided by the observed radio eclipses during a large fraction of the orbit (Ray et al. 2014, 2015). Thus, this implies a companion radius of $R_{\rm c} \approx 0.79\,R_\odot$, which we also adopt as fiducial value for the remainder of this discussion.

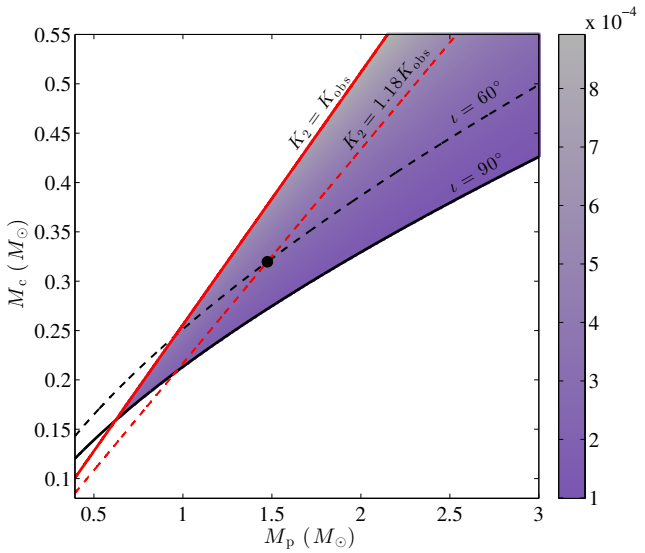

FIG. 2.— Mass-mass diagram for the PSR J2339–0533 binary system. The non-shaded region is excluded by the pulsar mass function from the gamma-ray timing solution since $\sin\iota \leq 1$ (lower exclusion region) and from the companion mass function based on the optical radial-velocity measurements (Romani & Shaw 2011) since $K_2 \geq K_{\rm obs}$ (upper exclusion region). Over the shaded (permitted) region, the color code shows how the fraction of the companion's luminosity $\Delta L/L$ of Equation (13) required by the gravitational quadrupole coupling model varies with the assumed component masses. The black dot indicates the fiducial values for the component masses assumed here, based on the optical lightcurve modeling by Romani & Shaw (2011).

The optical spectroscopy by Romani & Shaw (2011) also shows that the companion's spectrum resembles that of a late-type star. However, the above estimates suggest that the stellar companion is likely less dense than a main-sequence star of the same mass, which has also been found for other redback systems (Archibald et al. 2013; Li et al. 2014).

3.2. *Energetics and Irradiation*

From the measured LAT energy flux G_{100} (given in Table 1), we can obtain an estimate of the gamma-ray luminosity $L_\gamma = 4\pi d^2 G_{100} \approx 6.7 \times 10^{32}$ erg s^{-1}, assuming no geometric beaming correction. This leads to a gamma-ray conversion efficiency of $\eta_\gamma = L_\gamma/\dot{E} \approx 4\%$, not atypical compared to the MSPs studied in Abdo et al. (2013).

We can also estimate the effect of pulsar irradiation on the companion. Romani & Shaw (2011) inferred a companion-backside temperature of approximately 2800 K, which suggests an intrinsic luminosity of $L \approx 1.3 \times 10^{32}\,{\rm erg\,s^{-1}}$ ($0.034\,L_\odot$) based on the above estimated radius. The irradiation efficiency $\eta_{\rm irr}$ is often used to describe the fraction of the pulsar spin-down energy absorbed and converted into optical emission. Assuming the contribution of an isotropic pulsar wind to the companion's optical luminosity via re-radiation is $L_{\rm irr} = \eta_{\rm irr}\dot{E}R_{\rm c}^2/(4a^2) \approx 9.7 \times 10^{32}\eta_{\rm irr}\,{\rm erg\,s^{-1}}$, we find an efficiency of $\eta_{\rm irr} = L/L_{\rm irr} \approx 14\%$. This is within the range of

typical irradiation efficiencies as found for the systems investigated in Breton et al. (2013).

3.3. *Possible Causes for the Orbital Period Variations*

Generally, an observed rate of change in the binary orbital period, $\dot{P}_{\rm orb}$, may result from various physical effects as discussed in (Doroshenko et al. 2001; Lazaridis et al. 2011). The possible causes, most relevant regarding the time scale of our observations, can be summarized as

$$\dot{P}_{\rm orb} = \dot{P}^{\rm GW}_{\rm orb} + \dot{P}^{\rm D}_{\rm orb} + \dot{P}^{M}_{\rm orb} + \dot{P}^{\rm Q}_{\rm orb}\,, \tag{4}$$

including energy loss due to gravitational-wave emission ($\dot{P}^{\rm GW}_{\rm orb}$), changes due to Doppler shifts ($\dot{P}^{\rm D}_{\rm orb}$), mass loss from the system ($\dot{P}^{M}_{\rm orb}$), and gravitational quadrupole moment coupling ($\dot{P}^{\rm Q}_{\rm orb}$).

The term $\dot{P}^{\rm GW}_{\rm orb}$ in Equation (4) is the contribution due to gravitational-wave emission. For the case of circular orbits this is given by (Peters 1964),

$$\dot{P}^{\rm GW}_{\rm orb} = -\frac{192\pi}{5}\left[\frac{2\pi}{P_{\rm orb}}\,\frac{GM_{\rm c}}{c^3}\right]^{5/3}\frac{q}{(q+1)^{1/3}}\,, \tag{5}$$

where c denotes the speed of light. The resulting value for $\dot{P}^{\rm GW}_{\rm orb} \simeq -1.3\times10^{-13}$ s s^{-1} is about three orders of magnitude smaller than the measured values of $\dot{P}_{\rm orb}$, and hence unlikely to be the primary cause.

The term $\dot{P}^{\rm D}_{\rm orb}$ in Equation (4) represents the combined effect of proper motion (Shklovskii 1970) and Doppler shifts due to a changing distance to the binary system, e.g., from the Galactic acceleration or due to a massive third body:

$$\dot{P}^{\rm D}_{\rm orb} = \dot{P}^{\rm Shk}_{\rm orb} + \dot{P}^{\rm Gal}_{\rm orb} + \dot{P}^{\rm acc}_{\rm orb}\,. \tag{6}$$

Using the measured proper-motion values given in Table 1 and the radio-based DM distance of $d = 0.45$ kpc, one obtains

$$\dot{P}^{\rm Shk}_{\rm orb} = \frac{(\mu_\alpha^2\cos^2\delta + \mu_\delta^2)\,d}{c}\,P_{\rm orb} \simeq 1.8\times10^{-14}\,{\rm s\,s^{-1}}\,. \tag{7}$$

Contributions from the Galactic acceleration, $\dot{P}^{\rm Gal}_{\rm orb}$, are typically of similar magnitude (Lazaridis et al. 2009). An acceleration of the binary system caused by a massive third body is also highly unlikely. If that was the case, the pulsar spin period and period derivative would be affected in the same way. From the measured values in Table 1 we can estimate the maximum contribution of this effect by assuming the apparent spin-down is entirely due to acceleration: $(\dot{P}^{\rm acc}_{\rm orb}/P_{\rm orb}) = (\dot{P}/P) \simeq 5\times10^{-18}\,{\rm s^{-1}}$, implying $\dot{P}^{\rm acc}_{\rm orb} \simeq 10^{-14}$ s s^{-1}. Thus, overall the term $\dot{P}^{\rm D}_{\rm orb}$ is found to be more than four orders of magnitude smaller than the observed $\dot{P}_{\rm orb}$ value for PSR J2339–0533.

The term $\dot{P}^{M}_{\rm orb}$ in Equation (4) results from mass loss of the binary system. The spin-down luminosity of the pulsar irradiating the companion can drive mass loss at a rate $\dot{M}_{\rm c}$ from the companion through an evaporative wind. Taking the orbit to be circular and assuming no mass is lost from the pulsar, one obtains (Jeans 1924),

$$\dot{P}^{M}_{\rm orb} = -2\frac{\dot{M}_{\rm c}}{M}P_{\rm orb}\,, \tag{8}$$

where $M = M_{\rm c} + M_{\rm p}$ denotes the total mass of the system. Assuming that all of the radiative energy from the pulsar intercepted by the companion (for a presumed isotropic pulsar wind) is converted into mass loss from the system, this would imply a rate $\dot{M}_{\rm c} \simeq 2.0\times10^{-8}\,M_\odot{\rm yr}^{-1}$ (Stevens et al. 1992). Inserting this value into Equation (8) gives $\dot{P}^{M}_{\rm orb} \simeq -1.2\times10^{-11}$ s s^{-1}, which is more than an order of magnitude smaller in number than the measured $\dot{P}_{\rm orb}$. More realistically, adopting the 14% efficiency for this process as estimated in Section 3.2, one gets $\dot{M}_{\rm c} \simeq 2.8\times10^{-9}\,M_\odot{\rm yr}^{-1}$ and $\dot{P}^{M}_{\rm orb} \simeq -1.7\times10^{-12}$ s s^{-1}. This therefore appears unlikely to be the primary cause for the orbital variation observed.

The possible contributions to $\dot{P}_{\rm orb}$ considered so far seem unlikely to be able to account for the large $P_{\rm orb}$-variation measured. In addition, these processes generate monotonic changes, which cannot explain the alternating increase and decrease of $P_{\rm orb}$ observed. Hence this must be caused by the last term, $\dot{P}^{\rm Q}_{\rm orb}$, resulting from cyclic changes of the companion's gravitational quadrupole moment. In the following, we scrutinize the plausibility of this explanation, confronting a specific theoretical model with the observational data.

3.4. *Gravitational Quadrupole Coupling*

To explain the observed orbital-period modulation, the only plausible cause of those discussed above that remains is a changing gravitational quadrupole moment of the companion star (Matese & Whitmire 1983). Such gravitational quadrupole coupling (GQC) likely results from magnetic activity in the stellar companion (Applegate & Patterson 1987; Applegate 1992). Applegate & Shaham (1994) successfully applied the model by Applegate (1992) to the black widow pulsar binary PSR B1957+20, gravitationally coupling the orbital-period changes reported in (Arzoumanian et al. 1994) to changes in the quadrupole moment of the companion star. Similar $P_{\rm orb}$ variations on a time scale comparable to that found for PSR J2339–0533 were seen in another black widow system, PSR J2051–0827, and were also attributed to GQC (Doroshenko et al. 2001; Lazaridis et al. 2011). The transitional redback system PSR J1023+0038, which recently changed its state from MSP back to LMXB (Stappers et al. 2014), also displayed orbital-period changes at a comparable level (Archibald et al. 2013). Further fitting into this picture, notably analog orbital-period changes were found in long-term monitoring of LMXB systems (Wolff et al. 2009; Patruno et al. 2012), likely also caused by GQC arising from cyclic magnetic activity.

In Applegate's GQC model the companion star is magnetically active with a convective envelope and the pulsar is treated as a point mass moving in the gravitational field of the companion in a circular orbit. When the companion's gravitational quadrupole moment (due to tidal and centrifugal deformations) varies with time, this can cause a variable orbital motion at constant orbital angular momentum. When the companion becomes more oblate, its quadrupole moment increases, to balance gravitation the centripetal acceleration on the pulsar must increase, so that $P_{\rm orb}$ must decrease, and vice versa. Therefore, in principle any mechanism that can modulate the quadrupole moment of the companion also modulates the binary orbital period.

The specific mechanism suggested by Applegate (1992) considers cyclic, solar-like magnetic activity in the convective zone of the non-degenerate companion star. The magnetic field within the companion is assumed to generate a torque, which cyclically exchanges angular momentum between its outer convective layers and the inner part. Causing cyclic spin-up and spin-down of the companion's outer layers,

this leads to an oscillation of the oblateness and the gravitational quadrupole moment of the companion. When the outer layers spin up, the star becomes more oblate, the quadrupole moment increases and $P_{\rm orb}$ must decrease at fixed total orbital angular momentum. On the other hand, if the outer layers spin down, the quadrupole moment decreases, and $P_{\rm orb}$ increases.

Applegate & Shaham (1994) further hypothesized that tidal dissipation supplies the energy flows driving the convection in the rotating companion. The resulting magnetic activity and the mass loss due to the wind driven by pulsar irradiation contribute to a spin torque that holds the stellar companion slightly out of synchronous rotation giving rise to tidal dissipation and thus heats the companion internally.

Lanza et al. (1998) proposed an extension of Applegate's model. Instead of the internal angular momentum redistribution considered by Applegate (1992), they argued that a variation of the azimuthal magnetic field can also produce quadrupole moment changes. They invoked cyclic exchanges between kinetic and magnetic energy within the convective zone during the magnetic cycle to cause the modified distribution of angular momentum within the star.

To better estimate the duration of the magnetic activity cycle coupling to the observed orbital-period modulation of PSR J2339–0533, we compared the timing solution to the following simple model. We described the change in orbital frequency $\Delta f_{\rm orb}(t)$ around its nominal value (according to $P_{\rm orb}$ of Table 1) by a term linearly varying with time t (measured as difference from $T_{\rm ASC}$ in Table 1), and an oscillatory term with modulation period $P_{\rm mod} \equiv 1/\nu_{\rm mod}$ and derivative $\dot{P}_{\rm mod} \equiv -\dot{\nu}_{\rm mod}/\nu_{\rm mod}^2$,

$$\Delta f_{\rm orb}(t) = \dot{f}_{{\rm orb},\star}\, t + A \sin\left[2\pi\nu_{\rm mod} t + \pi\dot{\nu}_{\rm mod} t^2 + \psi\right] , \quad (9)$$

where A and ψ are the $P_{\rm orb}$-modulation amplitude and phase, respectively. Using chi-square minimization, the best-fit results we found for this modulation model along with their formal 1σ statistical uncertainties are given in Table 2. In particular, we estimated a modulation period $P_{\rm mod} = 4.2$ yr and a modulation amplitude $AP_{\rm orb}/(2\pi) = \Delta P_{\rm orb}/P_{\rm orb} = 2.3 \times 10^{-7}$. From the inferred value for $\dot{f}_{{\rm orb},\star}$ we derived the residual orbital-period derivative $\dot{P}_{{\rm orb},\star}$ given in Table 2. However, we caution that substantial systematic errors are expected, given that the reduced chi-square value of the fit was a few times greater than unity and secondary minima existed. Nonetheless, as illustrated in panel E of Figure 1, this model following Equation (9) allows one to qualitatively reproduce the observed orbital-period variation.

These results are to be compared to the GQC model, where a change in orbital period by $\Delta P_{\rm orb}$ is related to a change ΔQ of the companion's quadrupole moment Q via (Applegate & Patterson 1987),

$$\frac{\Delta P_{\rm orb}}{P_{\rm orb}} = -9\frac{\Delta Q}{M_{\rm c}\, a^2} . \quad (10)$$

While Q likely has a complex dependency on how mass, magnetic fields and rotational angular velocity are distributed within the star, it is dominated by the mass distribution in the outer layers of the companion where the centrifugal acceleration is largest. To estimate the resulting change ΔQ from the transfer of angular momentum to the outer part of the star, Applegate (1992) considered a thin shell of mass $M_{\rm s}$ and radius $R_{\rm c}$ whose angular velocity Ω will change by $\Delta\Omega$, giving

TABLE 2
ESTIMATED ORBITAL-PERIOD MODULATION MODEL PARAMETERS

Parameter	Value
Modulation amplitude, A ($\rm s^{-1}$)	$8.48(2) \times 10^{-11}$
Modulation period, $P_{\rm mod}$ (years)	4.15(1)
Modulation period derivative, $\dot{P}_{\rm mod}$ ($\rm s\ s^{-1}$)	–0.87(1)
Modulation phase, ψ (rad)	5.64(1)
Residual orbital-period derivative, $\dot{P}_{{\rm orb},\star}$ ($\rm s\ s^{-1}$)	$-1.57(2) \times 10^{-11}$

NOTE. — Numbers in parentheses are only statistical, formal 1σ uncertainties in the last digits.

(Applegate & Shaham 1994),

$$\frac{M_{\rm s}}{M_{\rm c}}\frac{\Delta\Omega}{\Omega} = \frac{GM_{\rm c}}{2R_{\rm c}^3}\,\frac{a^2}{R_{\rm c}^2}\,\frac{P_{\rm orb}^2}{4\pi^2}\,\frac{\Delta P_{\rm orb}}{P_{\rm orb}} . \quad (11)$$

Assuming corotation of the tidally locked companion, we obtain for the PSR J2339–0533 system,

$$\frac{\Delta\Omega}{\Omega} = 9.7 \times 10^{-7}\,\frac{M_{\rm c}}{M_{\rm s}} . \quad (12)$$

Applegate (1992) found observational results to be typically fit well for a shell of mass $M_{\rm s} \approx 0.1 M_{\rm c}$. Adopting this value here implies $\Delta\Omega/\Omega \approx 10^{-5}$. In Applegate's model, the magnetic field generation and angular velocity variation operates cyclically with period $P_{\rm mod}$ (the cycle of the orbital-period modulation). While no further details of this activity cycle were specified, Applegate (1992); Applegate & Shaham (1994) assumed that the energy needed for the transfer of angular momentum would require an associated change in the star's luminosity of

$$\Delta L = \frac{\pi}{3}\frac{G\,M_{\rm c}^2}{P_{\rm mod}}\,\frac{a^2}{R_{\rm c}^3}\frac{\Delta\Omega}{\Omega}\,\frac{\Delta P_{\rm orb}}{P_{\rm orb}} . \quad (13)$$

Using the above estimated value for $P_{\rm mod}$, the associated luminosity change is $\Delta L \approx 4.1 \times 10^{28}\,\rm erg\,s^{-1}$. This is only about 0.03% of the intrinsic luminosity of the companion, which we estimated in Section 3.2. Therefore, the companion should be easily capable of providing the required energy to power the orbital-period variations. Even if the true component masses were slightly different from those assumed, this conclusion remains robust. This is illustrated in Figure 2, where the required fractional luminosity is shown to vary by less than an order of magnitude over the permitted region in the mass-mass diagram.

For other classes of close binaries, such as the RS Canum Venaticorum systems, Lanza (2005) (and Lanza 2006) found a discrepancy of Applegate's GCQ model: The required surface angular velocity variations led to an energy dissipation rate in the turbulent convection zone of the secondary star exceeding the stellar luminosity. For PSR J2339–0533, with lower $\Delta P_{\rm orb}/P_{\rm orb}$ and $\Delta\Omega/\Omega$, this is not the case. Applying Equation (26) of Lanza (2006), we infer a ratio between the dissipated power and the stellar luminosity of only a few percent, further supporting Applegate's GCQ mechanism. However, if the true companion radius was much smaller than the one we assumed above, this energy balance could eventually become questionable. But this would also imply that the companion was actually not near filling its Roche lobe, which is currently not supported observationally (Romani & Shaw 2011).

Moreover, on the timescale of the observational data, the component masses and the orbital angular momentum are approximately constant as presumed by the GQC model. This implies that the observed orbital-period variation must also lead to a change in the orbital separation: $\dot{a}/a = 2\dot{P}_{\rm orb}/P_{\rm orb}$. Taking the largest $\dot{P}_{\rm orb}$ we observed, this would give $\dot{x} \simeq 2 \times 10^{-14}$ lt-s s^{-1}. This is still smaller than the measured upper limit on $\dot{x}$ provided in Table 1 and thus this aspect of the model is also in line with our timing measurements.

The above analysis of the orbital-period evolution (Table 2) indicates that aside from the modulation, a long-term change of $\dot{P}_{\rm orb,\star} \approx 10^{-11}$ s s^{-1} might still remain. If this residual orbital-period derivative was mostly due to mass loss, the next largest contribution as estimated in Section 3.3, then the rate would be $\dot{M}_{\rm c} \approx 2 \times 10^{-8} M_\odot {\rm yr}^{-1}$. To match this mass-loss rate the estimates made in Section 3.3 would require only little modification of the assumed irradiation efficiency or a slight deviation from the pulsar's presumed isotropic emission.

Overall, we conclude that the GQC theory offers a compatible explanation of the orbital-period variation observed for PSR J2339–0533.

4. CONCLUSIONS

Using the available *Fermi*-LAT data spanning more than six years, we carried out a precision gamma-ray timing analysis of the redback-type pulsar binary PSR J2339–0533. Most notably, the results revealed a long-term modulation of the 4.6-hour binary orbital period. We found that this observed phenomenon can be explained by variations of the gravitational quadrupole moment of the companion, through a mechnism proposed by Applegate (1992).

Since Applegate's model offers a compatible explanation, it implicates that the companion star must have a sizeable outer convective zone, where cyclic magnetic activity causes the quadrupole moment changes leading to the observed orbital-period modulation. Additional evidence for such convective fluctuations is provided by our measured residual orbital eccentricity, found to be higher than theoretically predicted for such a tight binary (Phinney 1992). The strong irradiation and possibly also the tidal interaction with the close-by pulsar may drastically affect the internal structure of the companion making it similar to that of a main-sequence low-mass star with a convective envelope. While its optical spectrum is in fact consistent with a late-type star (Romani & Shaw 2011), the companion however appears to be less dense than a main-sequence star of the same mass.

Combined with the pulsar ephemeris, future optical observations of the companion can help to more tightly constrain the system parameters, e.g., their component masses. As another interesting prospect, such measurements might also be able to provide evidence for a variation in accordance with stellar activity. This might also allow further tests of the gravitational quadrupole coupling theory, given the high timing precision with which we can measure the orbital-period variation. Ultimately, one might hope to identify the type of stellar magnetic dynamo in action or the physical origin of the differential rotation within the companion's convective layers, currently observationally difficult to access otherwise.

Surprisingly many black widow and redback pulsar binaries have been discovered in targeted radio searches of unidentified LAT sources. However, the fact that many of those systems also show significant radio eclipses and variations in their orbital parameters often makes it still extremely difficult to also detect the gamma-ray pulsations. That is because the short-term radio timing solutions cannot be extended immediately backwards to cover the full LAT data time span since *Fermi*'s launch. As demonstrated for PSR J2339–0533, the method presented here can help address this problem. Besides revealing the gamma-ray pulsations, by making full use of the great potential of the exquisite LAT data, this also opens the unique possibility for long-term monitoring and insights into the complex interplay of effects influencing the orbital evolution of such irradiating pulsar binary systems.

We thank fellow members of the LAT collaboration for helpful discussions and Lucas Guillemot, Massimiliano Razzano, Paul Ray, and Roger Romani for helpful comments on the manuscript. This work was supported by the Max-Planck-Gesellschaft (MPG), as well as by the Deutsche Forschungsgemeinschaft (DFG) through an Emmy Noether Research Grant, No. PL 710/1-1 (PI: Holger J. Pletsch).

The *Fermi* LAT Collaboration acknowledges generous ongoing support from a number of agencies and institutes that have supported both the development and the operation of the LAT as well as scientific data analysis. These include the National Aeronautics and Space Administration and the Department of Energy in the United States, the Commissariat à l'Energie Atomique and the Centre National de la Recherche Scientifique / Institut National de Physique Nucléaire et de Physique des Particules in France, the Agenzia Spaziale Italiana and the Istituto Nazionale di Fisica Nucleare in Italy, the Ministry of Education, Culture, Sports, Science and Technology (MEXT), High Energy Accelerator Research Organization (KEK) and Japan Aerospace Exploration Agency (JAXA) in Japan, and the K. A. Wallenberg Foundation, the Swedish Research Council and the Swedish National Space Board in Sweden.

Additional support for science analysis during the operations phase is gratefully acknowledged from the Istituto Nazionale di Astrofisica in Italy and the Centre National d'Études Spatiales in France.

REFERENCES

Abdo, A. A., et al. 2009, ApJS, 183, 46
—. 2013, ApJS, 208, 17
Acero, F., et al. 2015, arXiv:1501.02003
Applegate, J. H. 1992, ApJ, 385, 621
Applegate, J. H., & Patterson, J. 1987, ApJ, 322, L99
Applegate, J. H., & Shaham, J. 1994, ApJ, 436, 312
Archibald, A. M., et al. 2013, arXiv:1311.5161
—. 2009, Science, 324, 1411
Arzoumanian, Z., Fruchter, A. S., & Taylor, J. H. 1994, ApJ, 426, L85
Atwood, W. B., et al. 2009, ApJ, 697, 1071
Barr, E. D., et al. 2013, MNRAS, 429, 1633
Breton, R. P., et al. 2013, ApJ, 769, 108
Chen, H.-L., Chen, X., Tauris, T. M., & Han, Z. 2013, ApJ, 775, 27
de Jager, O. C., Raubenheimer, B. C., & Swanepoel, J. W. H. 1989, A&A, 221, 180
Doroshenko, O., et al. 2001, A&A, 379, 579
Eggleton, P. P. 1983, ApJ, 268, 368
Feroz, F., Hobson, M. P., & Bridges, M. 2009, MNRAS, 398, 1601
Jeans, J. H. 1924, MNRAS, 85, 2
Kerr, M. 2011, ApJ, 732, 38
Kong, A. K. H., et al. 2012, ApJ, 747, L3
Lange, C., et al. 2001, MNRAS, 326, 274
Lanza, A. F. 2005, MNRAS, 364, 238
—. 2006, MNRAS, 369, 1773
Lanza, A. F., Rodono, M., & Rosner, R. 1998, MNRAS, 296, 893
Lazaridis, K., et al. 2009, MNRAS, 400, 805

—. 2011, MNRAS, 414, 3134
Li, M., Halpern, J. P., & Thorstensen, J. R. 2014, ApJ, 795, 115
Matese, J. J., & Whitmire, D. P. 1983, A&A, 117, L7
Nice, D. J., Arzoumanian, Z., & Thorsett, S. E. 2000, in Astronomical Society of the Pacific Conference Series, Vol. 202, IAU Colloq. 177: Pulsar Astronomy - 2000 and Beyond, ed. M. Kramer, N. Wex, & R. Wielebinski, 67
Papitto, A., et al. 2013, Nature, 501, 517
Patruno, A., et al. 2012, ApJ, 746, L27
Peters, P. C. 1964, Physical Review, 136, 1224
Phinney, E. S. 1992, Royal Society of London Philosophical Transactions Series A, 39
Pletsch, H. J., et al. 2012, Science, 338, 1314
Ransom, S. M., et al. 2011, ApJ, 727, L16
Ray, P. S., et al. 2011, ApJS, 194, 17
—. 2012, arXiv:1205.3089
—. 2013, ApJ, 763, L13
Ray, P. S., et al. 2014, in American Astronomical Society Meeting Abstracts, Vol. 223, American Astronomical Society Meeting Abstracts, No. 140.07
—. 2015, in prep.
Roberts, M. S. E. 2013, in IAU Symposium, Vol. 291, IAU Symposium, ed. J. van Leeuwen, 127–132
Romani, R. W. 2012, ApJ, 754, L25
Romani, R. W., & Shaw, M. S. 2011, ApJ, 743, L26
Romani, R. W., et al. 2012, ApJ, 760, L36
Schwarz, G. 1978, AnSta, 6, 461
Shklovskii, I. S. 1970, Soviet Ast., 13, 562
Smedley, S. L., Tout, C. A., Ferrario, L., & Wickramasinghe, D. T. 2015, MNRAS, 446, 2540
Stappers, B. W., et al. 2014, ApJ, 790, 39
Stevens, I. R., Rees, M. J., & Podsiadlowski, P. 1992, MNRAS, 254, 19P
van Kerkwijk, M. H., Breton, R. P., & Kulkarni, S. R. 2011, ApJ, 728, 95
Wolff, M. T., Ray, P. S., Wood, K. S., & Hertz, P. L. 2009, ApJS, 183, 156